

Radial seismic anisotropy as a constraint for upper mantle rheology

Thorsten W. Becker^{a,*}, Bogdan Kustowski^b, Göran Ekström^c

^a Department of Earth Sciences, University of Southern California, Los Angeles, CA, USA

^b Department of Earth and Planetary Sciences, Harvard University, Cambridge MA, USA

^c Department of Earth and Environmental Sciences, Lamont-Doherty Earth Observatory, Palisades, NY, USA

Received 26 July 2007; received in revised form 9 November 2007; accepted 22 November 2007

Available online 8 December 2007

Editor: R.D. van der Hilst

Abstract

Seismic shear waves that are polarized horizontally (SH) generally travel faster in the upper mantle than those that are polarized vertically (SV), and deformation of rocks under dislocation creep has been invoked to explain such radial anisotropy. Convective flow of the upper mantle may thus be constrained by modeling the textures that progressively form by lattice-preferred orientation (LPO) of intrinsically anisotropic grains. While azimuthal anisotropy has been studied in detail, the radial kind has previously only been considered in semi-quantitative models. Here, we show that radial anisotropy averages as well as radial and azimuthal anomaly-patterns can be explained to a large extent by mantle flow, if lateral viscosity variations are taken into account. We construct a geodynamic reference model which includes LPO formation based on mineral physics and flow computed using laboratory-derived olivine rheology. Previously identified anomalous v_{SV} regions beneath the East Pacific Rise and relatively fast v_{SH} regions within the Pacific basin at ~150 km depth can be linked to mantle upwellings and shearing in the asthenosphere, respectively. Continental anisotropy at shallow (~50 km) depth is under-predicted, and these deviations are in quantitative agreement with the expected signature of frozen-in, stochastically-oriented anisotropy from past tectonic episodes. We also consider two end-member models of LPO formation for “wet” and “dry” conditions for the asthenosphere (~150 km). Allowing for lateral variations in volatile content, the residual signal can be much reduced, and the inferred volatile patterns underneath the Pacific appear related to plume activity. In deeper layers (~250 km), anisotropy indicates that small-scale convection disrupts plate-scale shear underneath old oceanic lithosphere. We suggest that studying deviations from comprehensive geodynamic reference models, or “residual anisotropy”, can provide new insights into the nature and dynamics of the asthenosphere.

© 2007 Elsevier B.V. All rights reserved.

Keywords: seismic anisotropy; radial anisotropy; mantle rheology; mantle convection; volatiles; continental formation

1. Introduction

Seismic shear waves that are polarized horizontally (SH), such as Love waves, travel faster on average in the upper mantle than those that are polarized vertically (SV), such as Rayleigh waves (Anderson, 1966). This observation implies a layer with radial seismic anisotropy where $v_{SH} > v_{SV}$ (Dziewoński and Anderson, 1981), and at sub-crustal depths anisotropy is likely caused by

flow alignment of olivine under dislocation creep (Nicolas and Christensen, 1987). Convection in the upper mantle may hence be constrained by modeling the textures that form by lattice-preferred orientation (LPO) of intrinsically anisotropic grains (e.g. Montagner, 1998). There are observations of transition-zone anisotropy (e.g. Wookey et al., 2002; Trampert and van Heijst, 2002), but most models agree that the majority of the upper mantle signal arises above ~250 km. This has been linked to the dominance of dislocation *vs.* diffusion creep at these depths (Karato, 1992; Gaherty and Jordan, 1995; Karato, 1998), and anisotropy may therefore constrain rheology (McNamara et al., 2002).

In the flow end-member model, anisotropy is caused by LPO that formed recently in mantle convection (10 to 100 Ma timescale). Alternatively, seismic anisotropy may be related to deformation

* Corresponding author. Department of Earth Sciences, University of Southern California, MC 0740, 3651 Trousdale Pkwy, Los Angeles, CA 90089-0740, USA. Tel.: +1 213 740 8365; fax: +1 213 740 8801.

E-mail address: twb@usc.edu (T.W. Becker).

over past tectonic episodes (100 Ma to 1 Ga timescale). Those might be frozen into the lithosphere, and in particular the continental crust and the strong roots beneath. How these two domains partition with depth and tectonic province, and what this implies for lateral viscosity variations (LVVs), is still debated (e.g. Gung et al., 2003; Conrad et al., 2007; Becker et al., 2007a; Fouch and Rondenay, 2006).

In boundary-layers, $v_{SH} > v_{SV}$ should be associated with shear-flow, such as underneath plates, and we expect $v_{SH} < v_{SV}$ for radial transport, such as underneath spreading centers or subduction zones (Chastel et al., 1993; Montagner, 2002). LPO will also be expressed as azimuthal anisotropy where v_{SV} depends on horizontal propagation orientation, and the fast orientations follow the direction of flow to first order (McKenzie, 1979; Tanimoto and Anderson, 1984; Silver, 1996). Geodynamic modeling has so far only addressed this aspect of anisotropy further (Tanimoto and Anderson, 1984; Gaboret et al., 2003; Becker et al., 2003; Behn et al., 2004). This lack of comprehensive geodynamic models is partly because more direct azimuthal observations, e.g. from shear-wave splitting, have been available for a long time, and partially because the computation of detailed forward models has only recently become feasible.

Mineral physics theories are able to reproduce laboratory results on the development of olivine LPO (Wenk and Tomé, 1999; Kaminski and Ribe, 2001). There is also now a growing body of laboratory work on how LPO is affected by water and deviatoric stress (e.g. Karato et al., in press). By combining insights from mineral physics and geodynamics, it may be possible to detect volatile variations in the asthenosphere (Karato, submitted for publication), and the associated depletion stiffening may be important on plume and plate length-scales (e.g. Ito et al., 1999; Lee et al., 2005). Regional models interpreting LPO texture exist (e.g. Chastel et al., 1993; Tommasi et al., 2000; Blackman and Kendall, 2002; Wenk et al., 2006), and LPO formation has also been tested in global flow, where it was found that the heterogeneity of the synthetic LPO textures matches that of mantle xenoliths (Becker et al., 2006a). The success of such studies lend confidence in our attempts to construct a forward model of anisotropy based on convective flow. If such a model is able to match the basic observables adequately, it can form a meaningful “reference” against which to test refinements.

Here, we ask how well both radial and azimuthal anisotropy can be matched by the reference model. We present the first geodynamic estimate of radial anisotropy, which has previously only been considered in semi-quantitative approaches (Regan and Anderson, 1984; Chastel et al., 1993; Montagner, 2002), and show that averages and anomalies at sub-lithospheric depths can be explained by mantle flow. By evaluating the discrepancies between seismology and geodynamics, “residual anisotropy”, quantitative insights into asthenospheric dynamics may be gained.

2. Methods

2.1. Seismological maps of anisotropy

While a complete description of upper mantle anisotropy is desirable (Montagner and Tanimoto, 1991), anisotropy is often

decomposed into special cases: Azimuthal anisotropy means that SV waves with azimuth Ψ in the horizontal obey a fast and a slow wave speed, $v_{SV}^{1,2}$, (“2 Ψ structure”)

$$\rho \left(v_{SV}^{1,2} \right)^2 = L \pm G_c \cos(2\Psi) \pm G_s \sin(2\Psi). \quad (1)$$

Here, ρ is density, and L and $G_{c,s}$ are linear functions of elasticity tensor components (Montagner and Nataf, 1986). If azimuthal anisotropy is absent, or averages are taken over all azimuths, anisotropy is termed radial (or: “transverse isotropy”). The elasticity tensor is then reduced to five parameters A , C , N , L , and F , which relate to velocities as (e.g. Dziewoński and Anderson, 1981)

$$\rho v_{PH}^2 = A, \quad \rho v_{PV}^2 = C, \quad \rho v_{SH}^2 = N, \quad \text{and} \quad \rho v_{SV}^2 = L, \quad (2)$$

with

$$\xi = \left(\frac{v_{SH}}{v_{SV}} \right)^2 = \frac{N}{L}, \quad \phi = \left(\frac{v_{PV}}{v_{PH}} \right)^2, \quad \text{and} \quad \eta = \frac{F}{A - 2L} \quad (3)$$

the shear (ξ) and compressional (ϕ) wave anisotropy, respectively. The ellipticity, η , determines the shape of the transition between v_{SH} and v_{SV} as a function of dip from the horizontal (Anderson, 1966). We use Voigt averaging throughout; the inherent assumption of constant strain is probably appropriate for seismic wave propagation, and relative variations in v_S can be approximated (for $\eta = 1$) by

$$\delta v_S \approx \delta v_S^{\text{Voigt}} = d \ln v_S^{\text{Voigt}} \approx (\delta v_{SH} + 2\delta v_{SV})/3. \quad (4)$$

The fact that PREM (Dziewoński and Anderson, 1981) already includes 1-D anisotropy with $v_{SH} > v_{SV}$ (Fig. 1a) is sometimes not appreciated; maps of 3-D variations in v_{SH} and v_{SV} are often with respect to an anisotropic reference. Regan and Anderson (1984) and Montagner and Nataf (1986) presented radial anisotropy models based on a tectonic regionalization and petrological information. Early models of 3-D radial anisotropy were discussed by Nataf et al. (1986), and Montagner and Tanimoto (1991) established a joint model of azimuthal and radial anisotropy. Since then, numerous upper mantle radial anisotropy models have been published (e.g. Ekström and Dziewoński, 1998; Shapiro and Ritzwoller, 2002; Zhou et al., 2006, and Table 1), employing different theory and inversion choices. Here, we will discuss what we perceive to be robust radial anisotropy patterns, and compare different seismological maps. We comment on four seismological models but focus on global ξ -maps from *S362WMANI* (Kustowski et al., submitted for publication) and *SAW642AN* (Panning and Romanowicz, 2006) (Table 1). Those two recent models have the advantage that they provide a consistent representation of both anisotropic and isotropic 3-D mantle structure.

Details of *S362WMANI* are described elsewhere (Kustowski et al., submitted for publication) and we only provide a short description here. In a first step, we inverted for a new reference model with layer-averages $\langle v_S \rangle$, $\langle v_P \rangle$, $\langle \xi \rangle$, $\langle \phi \rangle$, and, $\langle \eta \rangle$, allowing for independent variations of all of these parameters.

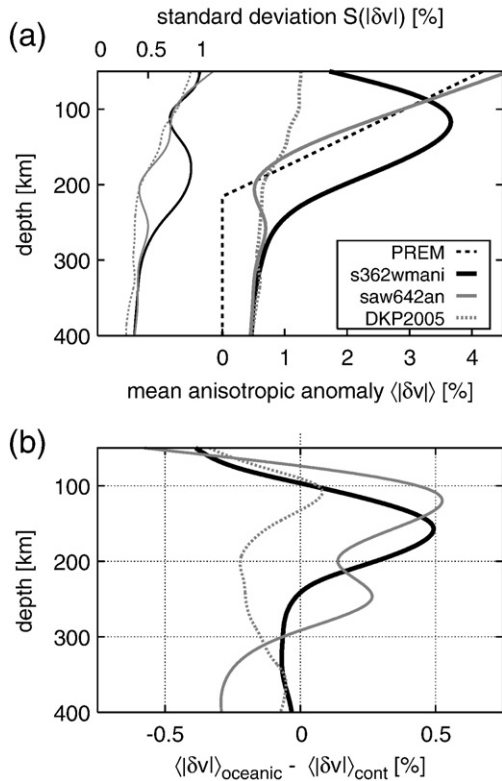


Fig. 1. Anisotropy strength in the upper mantle. (a): Global RMS heterogeneity (left) and mean (right) of absolute anisotropy amplitudes, $|\delta v|$, respectively. (b): Difference between mean $|\delta v|$ in oceanic and continental regions. We show radial anisotropy ($|\delta v| = |v_{SH} - v_{SV}|/v_S$, corresponding to $\langle \xi \rangle - 1$, see Fig. 4) from PREM, *S362WMANI* and *SAW642AN*. We also plot the azimuthal anisotropy ($|\delta v| = (v_{SV}^1 - v_{SV}^2)/\langle v_{SV} \rangle$, peak-to-trough) from *DKP2005* for amplitude comparison purposes. See Table 1 for model abbreviations.

The reference was then used to invert for isotropic, δv_S , and anisotropic, $\delta \xi$, velocity anomalies with nominal resolution of spherical harmonic degree $L \sim 18$. Because of limited δv_P resolution, we assumed $d \ln v_{PH} = 0.55 d \ln v_{SH}$, $d \ln v_{PV} = 0.55 d \ln v_{SV}$, and $d \ln \eta = 0$ (i.e. no lateral $\delta \eta$ anomalies). Geodynamic considerations are consistent with $d \ln v_{PV} \sim 0.55 d \ln v_{SV}$, but indicate $d \ln v_{PH} \sim d \ln v_{SH}$ (see Appendix A). We therefore tested factors of zero or unity, rather than 0.55, but found that those did not appreciably affect results.

Fig. 1a shows anisotropy strength against depth; radial anisotropy is from PREM, *S362WMANI*, and *SAW642AN*. Azimuthal anisotropy is shown for comparison and from *DKP2005* (Table 1), which is the only 3-D azimuthal anisotropy model that is available to us in electronic form. *S362WMANI* displays the strongest globally-averaged radial anisotropy, $\langle \xi \rangle$, at ~ 120 km (Fig. 1a), whereas both PREM and *SAW642AN* are characterized by monotonic increase of $\langle \xi \rangle$ from ~ 220 km toward the surface. (The differences between the arithmetic and geometric averages, appropriate for ratios as in Eq. (2), are $\lesssim 0.01\%$, and we report arithmetic averages for $\langle \rangle$ throughout.)

The question whether radial anisotropy reference models require a departure from PREM for $\langle \xi \rangle$ is debated (Beghein et al., 2006). However, based on several tests, we found that the new reference for ξ from *S362WMANI* is preferred by the data if we do not penalize deviations of $\langle \xi \rangle$ from PREM by means of

regularization. Variance reductions are systematically higher for our new 1-D reference model compared to PREM. Details of the $\langle \xi \rangle$ curve depend on parametrization, but a very similar depth-dependence of $\langle \xi \rangle$ was also inferred independently (Nettles and Dziewoński, 2008).

Azimuthal anisotropy is concentrated in the uppermost mantle (Tanimoto and Anderson, 1984; Montagner, 2002). In *DKP2005*, the RMS anomaly increases monotonously from 300 km to the surface (Fig. 1a), but the radial anisotropy RMS is stronger at all depths above ~ 200 km. This difference is more pronounced when RMS anomalies in oceanic and continental regions are separated (Fig. 1b). For *DKP2005*, the strongest oceanic signal is found at ~ 100 km depth where the anisotropy is mainly along the mid-oceanic ridges (Debayle et al., 2005). It is in this depth range and within oceanic regions that geodynamic anisotropy predictions are most similar to tomography (Becker et al., 2007b). At other depths, much of the anisotropy in *DKP2005* is in continental regions, and only the deep signal beneath Australia has been linked to asthenospheric shearing (Debayle et al., 2005). In contrast, radial anisotropy is relatively stronger in oceanic regions at all depths below the lithosphere (Fig. 1b). All models agree in that shallow structure at ~ 50 km depth is focused in the continental regions, which may be the signature of frozen-in anisotropy.

When anomaly maps for *S362WMANI* are considered (Fig. 2), $\delta v_S < 0$ underneath spreading centers at ~ 50 km appears associated with $\delta \xi > 0$, but there are no apparent correlations between anisotropy and isotropic anomalies at larger depths. Some of the $\delta \xi$ features in *S362WMANI* have been discussed before, including a pronounced, fast v_{SH} anomaly at ~ 150 km depth in the central Pacific close to Hawaii, where $\xi \gtrsim 1.1$ (Ekström and Dziewoński, 1998). Other features include the anomaly underneath the East Pacific Rise at 250 km depth, where $v_{SV} > v_{SH}$, presumably because of radial flow (Gu et al., 2005; Panning and Romanowicz, 2006). It has been shown that such anomalies are not due to inadequate 1-D sensitivity kernels (Boschi and Ekström, 2002), and lateral variations are also stable with respect to the potential interference of overtones, which complicate particularly Love phase velocity measurements (Nettles and Dziewoński, 2008).

Table 1
Seismological models analyzed

Model name	Type	Reference
<i>S36WMANI</i>	Harvard whole mantle δv_S and $\delta \xi$ model	Kustowski et al. (submitted for publication)
<i>SAW642AN</i>	Berkeley whole mantle δv_S and $\delta \xi$ model	Panning and Romanowicz (2006)
<i>NE07</i>	Harvard upper mantle δv_S and $\delta \xi$ model	Nettles and Dziewoński (2008)
<i>SAW16AN</i>	Berkeley upper mantle δv_S and $\delta \xi$ model	Gung et al. (2003)
<i>DKP2005</i>	Upper mantle δv_{SV} and 2Ψ model	Debayle et al. (2005)
<i>SMEAN</i>	Composite whole mantle δv_S average	Becker and Boschi (2002)

First four are radial anisotropy models based on surface waves, fifth is an azimuthal anisotropy model for v_{SV} , and last reference model is from an average of isotropic tomography.

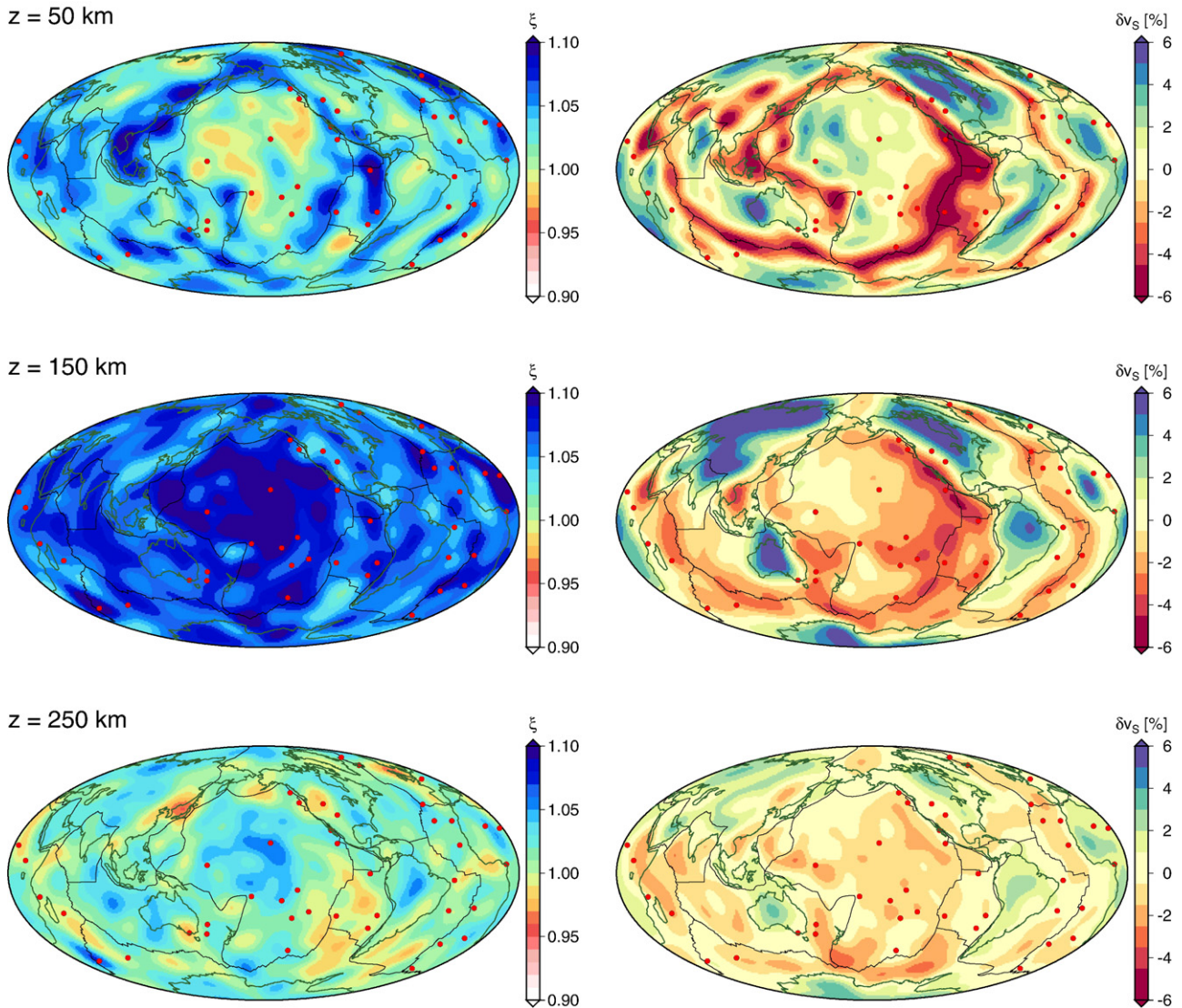


Fig. 2. Comparison of radial anisotropy (left; $\xi = (v_{SH}/v_{SV})^2$) and isotropic v_s anomalies (right) for *S362WMANI* at different depth levels as indicated. Note that ξ includes the (non-PREM like) average $\langle \xi \rangle$ of *S362WMANI* as shown in Fig. 1a. Red circles are hotspot locations from the compilation of Steinberger (2000).

Comparison of structure in different seismological models (Table 2) shows that isotropic maps are very similar, as expected. The mean correlation up to degree $L=8$ is $\langle r_8(\delta v_s) \rangle \approx 0.8$, both when compared among radially anisotropic models, and when compared to *SMEAN* (Becker and Boschi, 2002). The correlation for anisotropy is worse, $\langle r_8(\delta \xi) \rangle \approx 0.6$ within the Harvard and Berkeley models, but only $\langle r_8(\delta \xi) \rangle \approx 0.3$ when

maps from different groups are compared. Among the robustly mapped features is the Pacific $\delta \xi > 0$ anomaly.

Azimuthal anisotropy from *DKP2005* agrees with other Rayleigh-wave, phase-velocity maps at $r_8 \sim 0.47$ (Becker et al., 2007b). The correlations for radial are therefore only slightly better than those for azimuthal anisotropy, and the origin of these discrepancies is likely related to a, still poorly understood, combination of data selection, incomplete coverage, and inversion choices (e.g. Laske and Masters, 1998; Boschi et al., 2006; Trampert and Spetzler, 2006). It is therefore of interest to consider the predictions from forward models, which we describe next.

2.2. Geodynamical models

We construct models of radial anisotropy based on mantle circulation, making several simplifications, such as the neglect of feedback between LPO formation and viscosity (Christensen, 1987; Chastel et al., 1993). However, such models match several

Table 2

Average correlation of isotropic (δv_s , above diagonal) and radially anisotropic anomalies ($\delta \xi$, below unity diagonal, italic font) in the upper 350 km of the mantle, up to spherical harmonic degree $L=8$ for the models listed in Table 1

	<i>S362WMANI</i>	<i>NE07</i>	<i>SAW642AN</i>	<i>SAW16AN</i>	<i>SMEAN</i>
<i>S362WMANI</i>	1	0.89	0.86	0.86	0.91
<i>NE07</i>	<i>0.55</i>	1	0.80	0.80	0.86
<i>SAW642AN</i>	<i>0.28</i>	<i>0.29</i>	1	0.86	0.83
<i>SAW16AN</i>	<i>0.35</i>	<i>0.27</i>	<i>0.60</i>	1	0.87

geophysical observables (e.g. geoid, plate velocities), and were shown to be a better predictor of azimuthal anisotropy than shear in the “absolute plate motion” hypothesis (Becker et al., 2003), particularly underneath the oceanic plates (Becker et al., 2007b). Here, we put these models to another test by exploring radial anisotropy. Details are described in Becker et al. (2006a) and Becker (2006) and we only briefly summarize the approach and focus on improvements.

Mantle circulation is inferred from the instantaneous velocities of an incompressible, infinite Prandtl number fluid (Hager and O’Connell, 1981), and we solve the equations using the finite element code CitcomS by Moresi and Solomatov (1995) and Zhong et al. (2000). Flow is driven by plate velocities that are prescribed at the surface in the no-net-rotation reference frame, and by mantle density anomalies that are inferred by scaling δv_S with a constant factor of $d \ln \rho / d \ln v_S = 0.2$ (e.g. Becker et al., 2003). We verified that the forces are balanced; models with prescribed plate boundary geometries that are driven by density anomalies alone match the observed plate velocities (Becker and O’Connell, 2001; Becker, 2006). *S362WMANI* and *SAW642AN* were used as δv_S models for consistency, but other models such as *SMEAN* lead to very similar results with variations in model correlations typically smaller than ~ 0.05 , as expected from Table 2.

The viscosity, μ_r , profile of our starting model with only radial viscosity variations is in accordance with geoid constraints. A lithosphere down to 100 km with $\mu = 5 \cdot 10^{22}$ Pas overlies an asthenosphere with $\mu = 10^{20}$ Pas down to 410 km, after which 10^{21} Pas up to 660 km, where the viscosity jumps up to $\mu = 5 \cdot 10^{22}$ Pas (η_r model of Becker, 2006). For models with LVVs, the viscosity is an effective diffusion (μ_d) and dislocation (μ_D) creep rheology $\mu_{\text{eff}} = (\mu_d^{-1} + \mu_D^{-1})^{-1}$, where both μ_D and μ_d depend on temperature and pressure. We use laboratory values appropriate for dry olivine (Hirth and Kohlstedt, 2004), and all parameters are given in Becker (2006), η_{eff} case. The average viscosity structure of the upper mantle as in the starting μ_r can be broadly matched with μ_{eff} for a plausible choice of grain size of $d = 5$ mm. This parameter is the major control on the relative strength of μ_d vs. μ_D , and d is here assumed to be constant for simplicity. We do not mean to suggest that our choice of the LVV model is unique, as d might vary dynamically, and rheological measurements are still incomplete. However, our LVV flow model may serve as a first guess for “realistic” mantle flow fields, and leads to a better plate-tectonic fit than models without LVVs (Becker, 2006).

In order to make the models a more generic test of simple plate-tectonic flow, we modify the temperature structure that is inferred from δv_S in the shallowest mantle and lithosphere. For the top 100 km, we specify a half-space cooling profile based on seafloor age within oceanic plates (Conrad and Lithgow-Bertelloni, 2006). For the models with temperature-dependent viscosity, this leads to a lithospheric plate structure similar to that tested in Podolefsky et al. (2004). Underneath continents, stiff tectospheric roots are based on an equivalent lithospheric age based on interpretation of tomography with variable continental thickness (cf. Conrad and Lithgow-Bertelloni, 2006). However, we simplify the viscosity structure such that all sub-continental regions end up to be stiffer than sub-oceanic domains by a ~ 250

on average in the LVV model (Fig. 3). We found that extending the stiff sub-continental regions beyond the Archean areas used in Becker (2006) led to a focusing of radial anisotropy underneath the oceans that was preferred by the inversions (cf. Čadež and Fleitout, 2003). All continental regions above 250 km are assumed to be tectospheric (cf. Lee et al., 2005) where thermal anomalies are completely compositionally neutralized as in Becker (2006).

We assume that circulation is in steady-state for the time of LPO formation; this implies that models are most appropriate for the last ~ 10 Ma (Becker et al., 2006a). By tracking velocity gradients along streamlines, we then compute LPOs for an olivine(ol)–enstatite(en) assemblage (70/30%) using the DREX algorithm by Kaminski et al. (2004). As in that work, enstatite grains are assumed to not interact with olivine and mainly serve to reduce anisotropy from the single crystal values for olivine. With this mineral physics model, laboratory experiments on LPO development can be matched with a small number of parameters (Kaminski and Ribe, 2001), listed in Table 3.

We will focus on the low-stress, “dry” (low-water content), A-type LPO (in the nomenclature of Karato et al., in press). Texture development for A-LPO is best constrained by laboratory experiments and was used to calibrate the DREX (Kaminski et al., 2004) parameters. Karato et al. (in press) discuss how LPO formation depends on a range of parameters including temperature and pressure. Here, we will only consider volatile variations in the low deviatoric stress regime with $\lesssim 300$ MPa. In this case, one may expect a transition between dry (A) LPO, to damp (E), and further to wet (C) LPO at water contents of ~ 200 and ~ 800 ppm H/Si, respectively (Karato et al., in press).

Different patterns of LPO can be matched by modifying slip-system activity (Kaminski, 2002). We realize that important aspects of LPO saturation, particularly for hydrated systems, are still poorly constrained, or unknown. For our purposes it is, however, sufficient that the overall anisotropy predictions of saturated LPOs are similar to the laboratory results. Synthetic deformation experiments for C and E-type slip-systems with the choices of Table 3 yielded anisotropy estimates that are consistent with the independent calculations by Karato et al. (in press). In

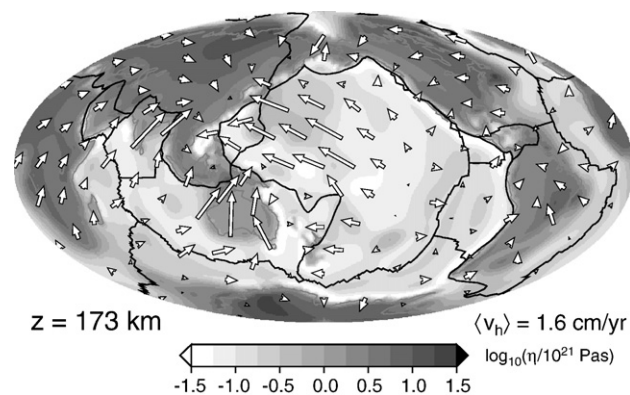


Fig. 3. Horizontal mantle flow (vectors, layer mean: ~ 2 cm/yr) and viscosity variations (background, \log_{10} of normalized viscosity) at ~ 170 km depth in our preferred flow model with lateral viscosity variations and a laboratory-derived, temperature-dependent, power-law viscosity (cf. Becker, 2006).

Table 3
Parameters used for the DREX LPO computations (cf. Kaminski et al., 2004)

Reference resolved shear stress					
LPO type	(010) [100]	(001) [100]	(010) [001]	(100) [001]	Reference
A, dry	1	2	3	∞	(Kaminski and Ribe, 2001)
E, damp	2	1	∞	3	Visual match of (Karato et al., in press)
C, wet	3	∞	2	1	(Kaminski, 2002, misprinted there)
High p	3	3	∞	1	Visual match of Mainprice et al. (2005)

A, E, and C refer to the low deviatoric stress regimes discussed by Karato et al. (in press) for different volatile content, “high p ” is the high-pressure LPO type suggested by Mainprice et al. (2005) for depths larger than ~ 200 km. “Visual match” means that we compared published orientation density plots to results from simple-shear synthetic experiments in order to derive the slip-system parameters for olivine by trial and error (cf. Kaminski, 2002). LPO development parameters: grain boundary mobility: 125; nucleation factor: 5, and boundary sliding threshold: 0.3; as in Kaminski et al. (2004).

particular, A and E-type LPOs show similar alignment patterns, but E has reduced amplitudes. In our tests, a single LPO-type forms everywhere, and there is no transition spatially. For our best-fit model at 150 km, the mean $\langle \xi \rangle$ values are then changed from $\langle \xi \rangle = 1.08$ for A to $\langle \xi \rangle = 1.05$ for E, *i.e.* $\sim 30\%$ anisotropy reduction ($v_{SH} > v_{SV}$). C-type fabrics orient such that the anisotropy is of opposite sign than for A ($v_{SV} > v_{SH}$), with $\langle \xi \rangle = 0.93$. We also briefly discuss a transition to high-pressure LPO formation that was suggested by Mainprice et al. (2005). For this, we modified the slip-system parameters from A at shallow depths to the high p values of Table 3 during advection if $p \geq 8$ GPa.

LPO is formed from initially random grain orientations by following tracers until a logarithmic saturation strain of ζ_c is reached at each location, if needed up to a maximum, cut-off age of 60 Ma. The ζ_c strain is then varied as a proxy for the degree of LPO saturation (Ribe, 1992). This approach is based on the result that $\zeta_c \geq 0.5$ is required to match the natural heterogeneity in xenolith LPOs and overprint possibly existing textures (Becker et al., 2006a). Anisotropy for the reference models is computed for all layers down to 410 km assuming LPO forms everywhere along streamlines. To allow evaluation of the suggestion that LPO anisotropy is controlled by the extent of dislocation creep, we use the partitioning between μ_d and μ_D from the LVV model, allowing a more consistent evaluation of anisotropy (McNamara et al., 2002; Podolefsky et al., 2004). Our best-fitting model uses the same streamlines as the regular LVV flow model, but LPO only forms when dislocation dominates over diffusion creep (cf. McNamara et al., 2002). This is implemented by scaling the non-rotational components of the velocity-gradient matrix by a factor $\delta = \dot{\epsilon}_D / (\dot{\epsilon}_D + \dot{\epsilon}_d)$, before using it to compute textures in DREX. Here, $\dot{\epsilon}_D$ and $\dot{\epsilon}_d$ are the second invariants of strain-rate in the dislocation- and diffusion creep viscosities, respectively. Existing texture is not destroyed or modified if material is in the diffusion creep regime ($\delta \sim 0$), but only rotated.

After LPO is estimated on 50 km spaced layers between 50 and 350 km, we perform a Voigt average of single crystal tensors taking only the depth-dependence of elastic moduli into account (see Appendix A). From the individual elastic tensors, we compute anisotropy ratios following Montagner and Nataf (1986) for azimuthal averaging. While the averaging properties of surface waves are likely more complex in detail, we assume that arithmetic averages of the local properties are appropriate, consistent with Voigt averaging for individual grains.

3. Results

3.1. Layer averages

We proceed to discuss radial anisotropy averages, and the joint global match of both radial and azimuthal anisotropy patterns. Fig. 4a shows a comparison of radial and azimuthal anisotropy with predictions from the starting flow model where viscosity varies only radially. The first row of Fig. 4 depicts layer averages of radial anisotropy, $\langle \xi \rangle$, and we denote the variations from the mean (RMS of $\delta \xi$ anomalies) with error bars. The χ^2 deviation between seismological and geodynamic averages is given in the legend and computed using the geodynamic model RMS as a standard error for $\langle \xi \rangle$. The second row of Fig. 4 shows how $\delta \xi$ variations from the mean correlate with *S362WMANI* globally up to spherical harmonic degree $L=8$, r_8 , and when restricted to oceanic plate regions. Dotted lines show global 95% and 99% significance levels for $(L+1)^2 - 2$ degrees of freedom, and the legend specifies the mean, global correlation between 50 and 350 km depth, $\langle r_8 \rangle$, as well as correlation at 200 km depth, r_8^{200} . The third row compares the average ellipticity parameter, $\langle \eta \rangle$, and, lastly, the fourth row shows correlations of azimuthal anisotropy 2Ψ patterns from *DKP2005* in analogy to the second row. Significance levels are given for $(L-1)(2L+6) - 2$ degrees of freedom (generalized spherical harmonics are used for 2Ψ correlations; cf. Becker et al., 2007b).

All parameters for the starting model in Fig. 4a are as in earlier best-fit models for plate-velocity and azimuthal anisotropy inversions (Becker et al., 2003), with the exception that we used Voigt averaged, isotropic v_S anomalies *S362WMANI* to infer density anomalies for consistency. Also, texture is computed up to $\zeta_c = 0.75$ saturation strain, and LPO formation is assumed to be active, and of A-type, everywhere within the top 410 km of the mantle. Without lateral viscosity variations, relatively homogeneous shear in the uppermost mantle results (Becker et al., 2003). Deep radial anisotropy is clearly over-predicted for this model, both in terms of ξ and η , as imaged by *S362WMANI*. The correlation with ξ -patterns is weak, and globally only slightly above the 99% significance level at ~ 200 km depth, where $r_8^{200} = 0.3$. Azimuthal anisotropy from *DKP2005* is matched above the 99% confidence level for depths shallower than ~ 200 km, and correlations are better within oceanic regions, consistent with earlier analyses of Rayleigh phase velocity maps (Becker et al., 2007b).

Fig. 4b shows anisotropy for a computation with LVVs of magnitude and distribution similar to what may be expected in the Earth, using the dislocation–diffusion creep law for dry

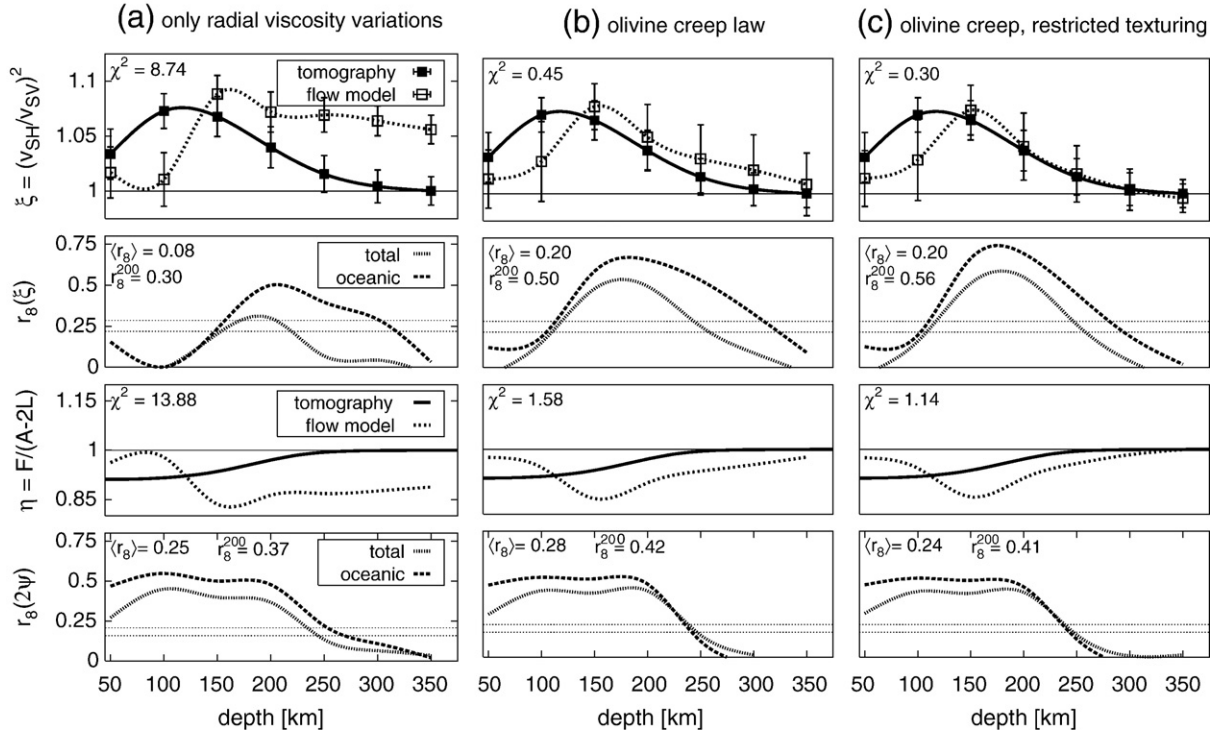


Fig. 4. Comparison between radial anisotropy (*S362WMANI*), azimuthal anisotropy (*DKP2005*, see Table 1) and geodynamic models. 1st row: Radial anisotropy layer averages (ξ) and RMS of $\delta\xi$ variations from the mean (shown as error bars). 2nd row: correlation of radial anisotropy patterns, $r_8(\xi)$. 3rd row: Average ellipticity (η). 4th row: azimuthal anisotropy correlation, $r_8(2\Psi)$. Dashed lines for r_8 indicate 95% and 99% significance levels; legend also specifies χ^2 misfits for ξ and η , as well as mean correlation $\langle r_8 \rangle$ and correlation at 200 km depth, r_8^{200} , for $r_8(\xi)$ and $r_8(2\Psi)$. (a): LPO predictions from a geodynamic model with only radial viscosity variations, (b): lateral viscosity variations from a joint dislocation/diffusion creep law for olivine, and (c): predictions from olivine creep law with LPO formation limited to regions dominated by dislocation creep.

olivine. The χ^2 misfit for $\langle \xi \rangle$ is strongly reduced compared to the radial viscosity model, but we now over-predict the seismically imaged RMS variations of $\delta\xi$. Azimuthal anisotropy amplitudes (not shown) are also over-predicted by the geodynamic model. Compared to $\sim 1\%$ G/L anomalies (Eq. (1)) in *DKP2005*, we estimate anomalies of $\sim 3.5\%$. However, our amplitudes are closer to those found by Montagner (2002), which we read off his maps as up to $\sim 2.5\%$ at 100 km depth. Moreover, we were able to fit *SKS* splitting delay times for the western United States with our flow models (Becker et al., 2006b), and the equivalent delay time of 200 km thick, constant 3% G/L anomaly is close to the globally observed mean of ~ 1.3 s. This discrepancy between *SKS* delay times and global azimuthal anisotropy models was noted and discussed by Debayle et al. (2005), and its origin remains to be determined. We will focus our further analysis on patterns rather than amplitudes, since we consider $\langle \xi \rangle$ misfits and correlations between radial and azimuthal anisotropy patterns more robust than the $\delta\xi$ RMS or azimuthal anisotropy amplitudes. The latter are expected to be more strongly affected by the inversion choices such as damping, and data coverage.

The LVVs in the model of Fig. 4b lead to focusing of anisotropy at ~ 150 km depth, which is expected given the relatively low asthenospheric viscosity that results from the pressure, temperature, and strain-rate dependence of the creep law (Fig. 3). However, the model with LVVs also shows

improved correlations with $\delta\xi$ anomalies; r_8 is above the 99% confidence level within a ~ 150 km wide, asthenospheric zone around ~ 175 km depth, and $r_8^{200} = 0.5$. This improvement in r_8^{200} is statistically significant at the 86% level using Fisher's z statistics. Correlations with azimuthal anisotropy are only moderately affected by the introduction of LVVs and how significant regional mismatches are is unclear (Becker et al., 2006a). The r_8 correlation for the LVV model compared with 2Ψ from *DKP2005* is slightly improved, with $r_8^{200} = 0.42$, compared to $r_8^{200} = 0.37$ for Fig. 4a.

The $\langle \eta \rangle$ (ellipticity) parameter curves in Fig. 4b are also now closer to the range that is imaged by seismology. We discuss petrological and geodynamical scaling relationships for variations in ϕ , ξ , and η in the Appendix A, and find that variations in these anisotropy ratios are generally predicted to be highly correlated. This motivates using petrological scaling parameters in seismological inversions (Montagner and Anderson, 1989; Becker et al., 2006a). Surface waves are inherently not very sensitive to ϕ and η for upper mantle maps and, in particular, different $\langle \eta \rangle$ reference profiles may be permitted by the data (Beghein et al., 2006). However, the radial average $\langle \eta \rangle$ of *S362WMANI* was derived without assuming any scaling relationship between P and S anomalies. The observation that $\langle \eta \rangle$ from seismology broadly agrees with the geodynamic estimates (Fig. 4b) therefore confirms the consistency of the new $\langle \eta \rangle$ reference model with petrological expectations.

By comparing Fig. 4a and b, we conclude that the introduction of LVVs has led to a significant improvement in the fit to radial anisotropy, most clearly seen by the improvement in misfit for $\langle \xi \rangle$, and the increased correlation of anisotropy patterns at asthenospheric depth. Fig. 4c shows the results from our preferred model, which are based on the same flow model as Fig. 4b. However, LPO texturing is only active in those regions where dislocation dominates over diffusion creep. This makes the flow models more consistent with the microscopic processes of anisotropy formation, including global, spherical power-law flow. We find that the $\langle \xi \rangle$ misfit is slightly improved further by reduction of deep anisotropy, correlation with $\delta \xi$ at asthenospheric depths is also improved, to $r_8^{200} = 0.56$, but the match to azimuthal anisotropy slightly degrades. We will proceed to use the restricted texturing model of Fig. 4c as our “best-fit” model but all of our main conclusions in the remainder could be arrived at using patterns from the model in Fig. 4b.

In the asthenosphere, most of the improvement between models in Fig. 4a and b, or c, is due to the low viscosity asthenosphere underneath oceanic plates (Fig. 3), which leads to an efficient shear, alignment of LPO, and formation of radial anisotropy. This might as such not surprise, but the correlations with radial anisotropy are statistically highly significant at asthenospheric depths, with $r_8^{200} \sim 0.5$. This match with *S362WAMNI* is

comparable or better than the agreement amongst seismological maps (Table 2). Yet, importantly, the geodynamic model is significantly correlated with all seismological models, as is the case for azimuthal anisotropy (Becker et al., 2007b). We therefore consider the seismic structure as inferred from the flow model of Fig. 4c as a good first guess for a geodynamic reference. The remaining discrepancies between the geodynamic reference model and seismology, such as at shallow depths, can be used to explore how the Earth might deviate from the recent plate-tectonic flow scenario on which our geodynamic model is based.

3.2. Radial anisotropy patterns

Fig. 5 shows map comparisons of geodynamical predictions from our preferred model as in Fig. 4c, ξ -structure from *S362WAMNI*, and the difference between the two. Many of the broad scale features at 150 km depth and below are similar, as expected from the correlation values in Fig. 4. This includes the predictions of a $\delta \xi < 0$ region beneath the East Pacific Rise (Gu et al., 2005), and a $\delta \xi > 0$ anomaly within the Pacific basin that was as of yet unexplained (Ekström and Dziewonski, 1998). The latter anomaly is, however, much broader in the geodynamic model than in the seismologic maps. When $\delta \xi$ patterns in the different seismological models in Table 1 are considered, the

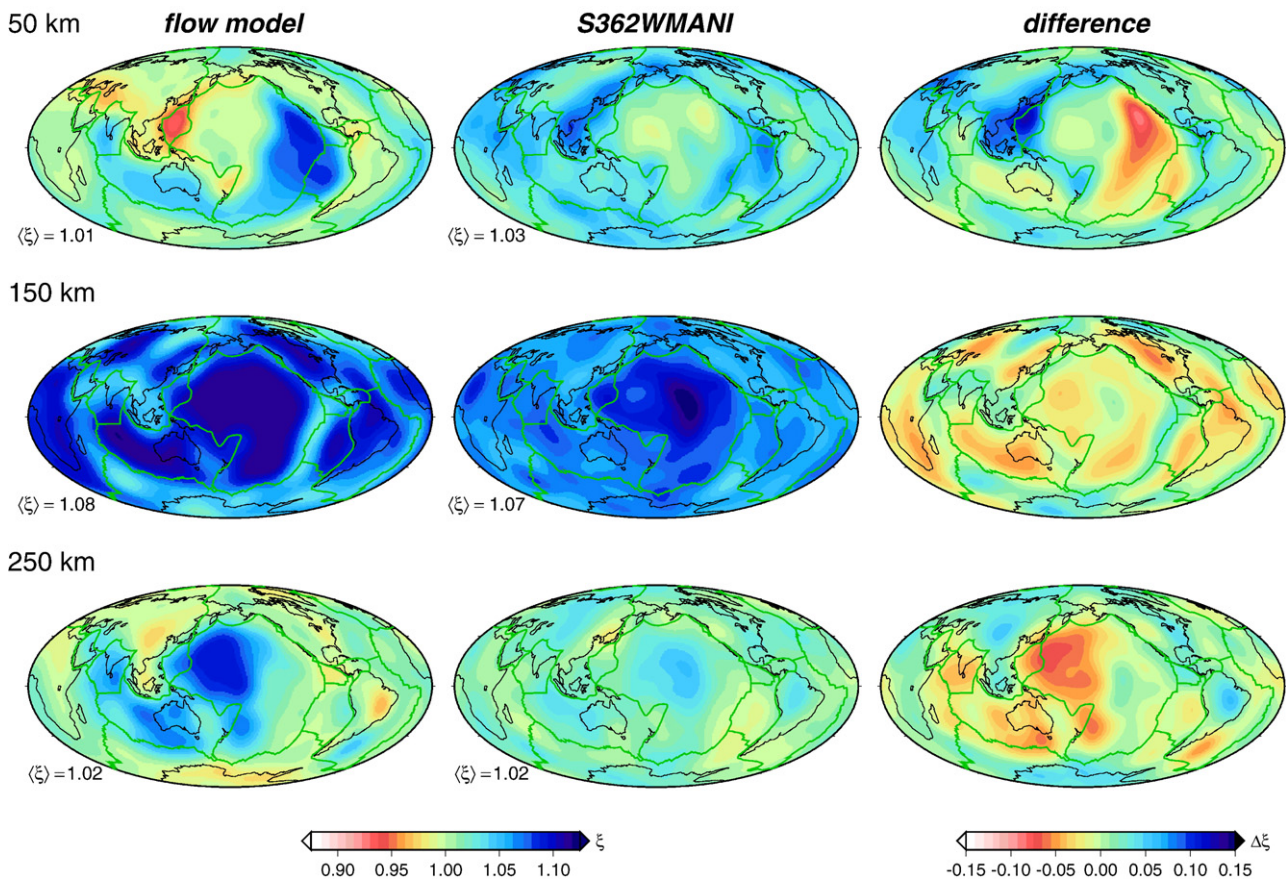


Fig. 5. Radial anisotropy as predicted by our reference flow model (left column, as used in Fig. 4c), as imaged by seismology (center column, *S362WAMNI*), and difference between seismology and model, $\Delta \xi$ (right column, “residual anisotropy”, where $\Delta \xi > 0$ means that v_{SH} is relatively faster than v_{SV} in seismology than in geodynamics). We show ξ anomalies (including the radial averages, indicated by $\langle \xi \rangle$ averages in the plot legends) at the indicated depths. All models were expanded up to $L=20$.

Pacific $\delta\xi > 0$ anomaly is the most important feature that is expected from geodynamic models and imaged across models.

To explore quantitatively the overall misfit for different geodynamic models, we conducted ~ 110 experiments varying parameters such as ζ_c (from 0.5 to 2), LVV structure underneath continents, and input density models (e.g. using *SAW642AN* δv_S to drive flow instead of *S362WMANI*). For *SAW642AN*, the mean amplitude misfit from the radial average, $\langle \xi \rangle$, is ~ 0.02 , as we always under-predict the PREM-like 1-D structure of *SAW642AN* (Fig. 1a). This compares to \sim zero overall radial anisotropy misfit for all considered models when compared to *S362WMANI*. Anisotropy strength is mainly controlled by the ζ_c strain which determines the degree of LPO saturation (Ribe, 1992; Becker et al., 2006a). Models with $\zeta_c \sim 0.75$ lead to the best match of radial $\langle \xi \rangle$ averages, regardless of density model, if $\delta\xi$ patterns are to be matched jointly with amplitudes. Values of $\zeta_c \geq 0.5$ are consistent with the degree of LPO variation that is required by variability of natural xenoliths (Becker et al., 2006a). However, there are many uncertainties about LPO formation and, importantly, the preservation of LPO once flow is in the diffusion creep regime. Here, we assume that all LPO remains frozen-in at diffusion creep-dominated depths, which are $\lesssim 50$ km (Podolefsky et al., 2004; Becker, 2006), and the shallow ξ predictions are only approximate. In addition to wet LPO formation, discussed below, we also experimented with suggested high-pressure slip systems (Mainprice et al., 2005) because those may strongly affect the deep anisotropy strength (Table 3). As expected, resulting anisotropy amplitudes and correlation decreased rapidly at depths ≥ 270 km. However, results at shallower depths were very similar to those of Fig. 4, and the depth-localization by means of dislocation/diffusion creep strain-rate partitioning appears a stronger control on radial anisotropy averages.

Our mantle flow models include several simplifying assumptions, such as isotropic viscosity and steady-state flow. The detailed patterns of radial anisotropy and the depth-dependence of the average anomalies moreover depend on the LVVs and the assumed rheology (McNamara et al., 2002). The latter is, however, a strength of the models that can be exploited. For example, the partitioning between the dislocation and diffusion creep laws affects the $\langle \xi \rangle$ predictions. The diffusion creep viscosity in turn depends on grain size, which is not well known and may well vary with depth. As Fig. 4c shows, employing constant grain size and dry olivine creep law parameters leads to a partitioning of anisotropy formation that is compatible with a range of observations. Alternatively, if grain size is constantly adjusting itself so that diffusion and dislocation creep are equi-partitioned (e.g. de Bresser et al., 2001; Hirth and Kohlstedt, 2004), another mechanism for the origin of radial anisotropy patterns as in Figs. 4 and 5 may need to be invoked.

Upper mantle averaged correlations from 100 to 300 km depth for $\delta\xi$ patterns between the geodynamic model ensemble which we considered and *S362WMANI* (cf. Fig. 4) were higher than for *SAW642AN* by ~ 0.15 for r_8 . The mean/maximum oceanic-region r_8 was 0.29/0.49 compared to 0.14/0.3, respectively, including those flow models which were driven by isotropic density structure as inferred from *SAW642AN*. Mean and maximum ensemble model correlations for oceanic regions are very similar between

NE07 and *S362WMANI*, but higher in the upper mantle Berkeley model *SAW16AN* (0.29/0.46) than for *S362WMANI*. Even accounting for differences in radial anisotropy averages, anisotropy patterns as imaged by our whole mantle *S362WMANI* are significantly closer to the geodynamic reference structures than those imaged by *SAW642AN*. We will therefore only use *S362WMANI* for further interpretation below.

4. Discussion

The most apparent mismatch of our models and the seismological maps occurs at lithospheric depths of 50 km where we also under-predict $\langle \xi \rangle$, while azimuthal anisotropy correlation remains at levels of ~ 0.4 throughout a broader range of the upper mantle (Fig. 4c). The geographic distribution of the difference in ξ -structure, $\Delta\xi$, which we term “residual anisotropy”, indicates that most of the mismatch occurs in continental regions where seismology indicates $v_{SH} > v_{SV}$, whereas the geodynamic model has either very little radial anisotropy, or even $v_{SH} < v_{SV}$. This is mainly because the high viscosity underneath the continental plates does not allow convective anisotropy to form with the cut-off advection time (Fig. 3); the surface limitation to LPO formation in dislocation creep does not have a large effect (Podolefsky et al., 2004; Becker, 2006).

We interpret this finding such that radial anisotropy in the lithosphere is dominated by frozen-in anisotropy which is not related to shearing in mantle flow. While the geographic association of the mismatch at 50 km with continental regions is already apparent from Fig. 5, it is useful to explore the ξ -amplitudes of suggested non-convective anisotropy further. We argued that a stochastic medium provides a good description of global *SKS* measurements within continental regions (Becker et al., 2007a), and determined horizontal correlation lengths of ~ 1600 km in Precambrian or Phanerozoic platforms of the tectonic regionalization GTR-1 (Jordan, 1981), compared to orogenic and magmatic zones with lengths of ~ 600 km. This finding was interpreted such that older continental regions record large-scale, super-continental collision type events, while anisotropy under younger continents with thinner lithosphere is affected by smaller-scale flow. As a test for residual radial anisotropy at 50 km as in Fig. 5, we therefore compute random vector fields with horizontal correlation lengths of 1600 km and align our ol/en single crystals with those vector orientations within Phanerozoic or Precambrian regions in GTR-1, assuming that we cannot access the related frozen-in anisotropy with our flow model.

The ξ -structure based on averaging 1000 of such random models is shown in Fig. 6, and is clearly very similar to the input regions that were identified as of “old” tectonic age. However, it is interesting that the resulting radial anisotropy amplitudes $\xi \sim 1.08$ are consistent with those that are imaged in Fig. 6, where residual anisotropy at 50 km indicates $\Delta\xi \sim 0.1$ within continents. In nature, tectonic processes will impose orientational anisotropy, such as layering, and a different type of averaging will also be performed by surface wave propagation. Yet, even for single random realizations, the SH signature of the individual vector fields is similar to Fig. 6. Residual anisotropy at 50 km correlates with the stochastic continental anisotropy model at the $r_8 = 0.32$

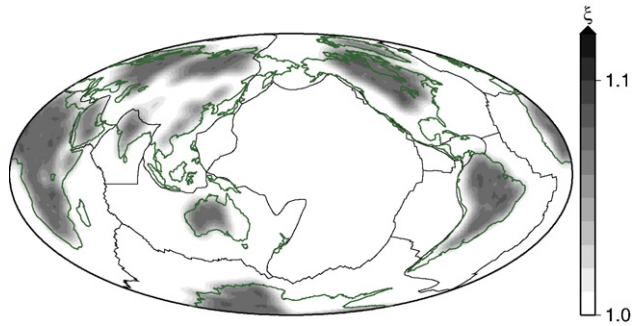


Fig. 6. Model of non-convective (frozen-in) radial anisotropy based on randomly oriented anisotropy, applying only in Phanerozoic and Precambrian platforms and shields (Jordan, 1981). Obtained by averaging 1000 realizations of a stochastic medium where our single crystal ol/en mix is oriented according to a single-layer vector field with exponential correlation function, and horizontal correlation length of 1600 km (Becker et al., 2007a).

and $r_8=0.58$ levels globally for *S362WMANI* and *NE07*, respectively. ($r_8=0.39$ and $r_8=0.31$ levels for *SAW642AN* and *SAW16AN*, respectively), which is significant at the 95% level. Also, it is expected that *NE07* should have better-resolved ξ structure underneath continents because of the use of regionalized sensitivity kernels and different data (Nettles and Dziewoński, 2008). Residual anisotropy within the lithospheric layer of Fig. 5 can therefore plausibly be explained by frozen-in structure in old continental regions, in terms of amplitude, and to some degree in terms of patterns. The sub-continental anisotropy is quite sensitive to the choices of the imposed stiff root structure (Becker, 2006). Future work should therefore explore how modified keel depths and locations could improve the radial anisotropy match (cf. Gung et al., 2003).

At asthenospheric depths of ~ 150 km, the agreement between geodynamic and seismological radial anisotropy patterns is best (Fig. 4b and c), and residual anisotropy amplitudes subdued (Fig. 5). Given that convective shear, and therefore geologically-recent anisotropy formation by mantle flow, should be the dominant anisotropy generator at these depths, at least underneath oceanic plates, the question arises what the source of the remaining discrepancies is. Clearly, the geodynamic model might be plain wrong. Given the promising performance of such mantle flow models for a range of geophysical observables, we think it is more likely that the model is relatively robust, and adjusting parameters such as the rheology or density model will only lead to minor differences. We therefore suggest that part of the residual anisotropy might be caused by LPO formation with fabrics other than that of A-type (Karato et al., in press). In particular, melting processes underneath mid-oceanic ridges and mid-plate, plume disturbances might affect the hydration levels of the asthenosphere (Lee et al., 2005; Karato, submitted for publication).

To provide a test of the potential signature of variations in LPO formation, we computed LPO as for the dry, A case in Fig. 5 but using damp, E-type, or wet, C-type slip systems (Table 3). In nature, LPO fabrics will depend on the transition between slip-system activity in a complicated way as a function of volatile and stress conditions present during advection (Kaminski, 2002; Lassak et al., 2006; Karato et al., in press). However, here we will assume, for simplicity, that the saturated LPO patterns

computed by using the same LPO formation-system everywhere represent end-member cases of radial anisotropy. Given that E-type radial anisotropy is highly correlated with A, but of smaller amplitude, we will only consider A and C-types quantitatively. Maps of ξ from C-LPO are very much mirror images of the ξ -anomalies for A-LPO in Fig. 5; regions of predominantly radial flow such as underneath the East Pacific Rise show $\xi \lesssim 1$ for C-LPO, and plate-scale shear underneath the Pacific plate leads to $\xi \sim 0.95$ with layer average $\langle \xi \rangle = 0.92$, i.e. $v_{SH} < v_{SV}$. This is the opposite of what is observed, and correlations with *S362WMANI* are correspondingly $r_8 = -0.42$ at 150 km, compared to $r_8 = 0.54$ for A-LPO and the reference flow model.

Volatile (water) content serves to partition the phase-diagram of LPO formation between A, E, and C-types at moderate deviatoric stress levels (Karato et al., in press). We will hence make the further assumption that a linear mixing between A and C-LPO based ξ -anomalies can provide a proxy for degree to which textures at certain geographic regions are affected by deviations from the dry anisotropy formation regime. We define a mixing ratio f , where $f=0$ (“dry”) and $f=1$ (“wet”) means purely A and C-based ξ -values as estimated from the local LPO of models run with purely A or C-type LPO, respectively. This is clearly only a rough approximation, among the complicating factors we neglect are the interactions of existing deformation fabrics that undergo a transition of slip-system activity with LPO formation. However, for a seismic wave Voigt averaging over a volume of material that exhibits anisotropy originating from different types of LPOs, linear mixing of elasticity constants as inferred from different LPO should be a useful first guess.

To invert how much of a C-type fabric would be required to explain the residual, radial anisotropy at 150 km depth as in Fig. 5, we first convert radial anisotropy into log-space, $r = \log(\xi)$, anomalies, because ξ is a ratio of moduli N/L . The anomalies at each layer for tomography, r_T , and A and C-LPO predictions, $r_{A,B}$, are then converted into a spherical harmonics expansions, expressed as a vector \hat{r} , with maximum degree $L=16$. We next solve

$$|\hat{r}_C \cdot \hat{f} - (\hat{r}_T - \hat{r}_A)| = 0 \quad \text{with} \quad f_i \geq 0 \quad (5)$$

for \hat{f} in a least-squares sense using a non-negative, least-squares (NNLS) algorithm ($\hat{r}_T - \hat{r}_A$ is the spectral representation of the residual anisotropy). The r_A and r_C anisotropy types are subsequently recombined such that the spatial expansion for the best-fit mixing fractions f is restricted to lie within $0 \leq f \leq 1$ everywhere (there are limited regions where the NNLS solution of Eq. (5) would lead to spatial f values larger than unity or smaller than zero).

Fig. 7 shows the predicted ξ -anomalies of the model that allows for a mix of dry A and wet C-type anisotropy, which now correlates with the seismological map (Fig. 5) at $r_8=0.81$ level, compared to $r_8=0.54$ for A-LPO alone. A and C-type LPO models for ξ are “orthogonal” to each other in an inverse-theory sense, as they span the range from $\xi > 1$ to $\xi < 1$ for the same general LPO alignment with flow. A general improvement in model-fit by adding additional free parameters, e.g. through the

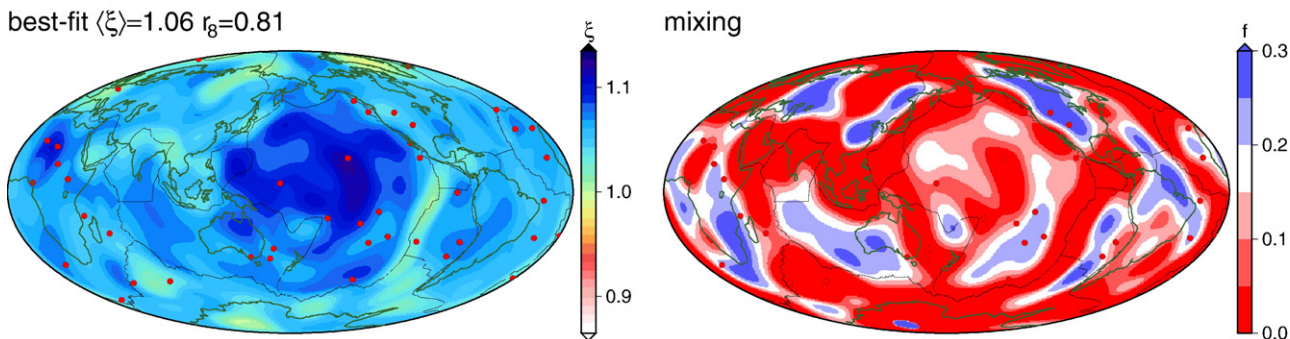


Fig. 7. Best-fit combined model of A+fC-type ξ -anisotropy at 150 km (left, compare with *S362WMANI* in Fig. 5) obtained by inverting the residual anisotropy of Fig. 5 for a non-zero fraction f of C-type anisotropy (right), which may serve as a proxy for volatile content (cf. Karato et al., in press). Left figure legend gives mean $\langle \xi \rangle$ and correlation with seismology.

mixing ratio f , is therefore not surprising. However, it is intriguing that moderate variations of $f \lesssim 0.3$ from the dry, A case are sufficient to improve the correlation of $\delta\xi$ substantially, affect the mean $\langle \xi \rangle$ very little, and reduce the residual anisotropy to $\langle \Delta\xi \rangle = 0.01$. Remaining regions of deviation are, e.g. underneath the East Pacific Rise, where even the combined model predicts smaller ξ than *S362WMANI*.

Another encouraging result is that the inferred best-fit f distributions (as shown in Fig. 7) are consistent among inversions obtained based on different seismological models. For example, $r_8 = 0.91$ for f between *S362WMANI* and *NE07*, respectively. C-type LPO saturation is not well constrained from laboratory measurements, and seismological ξ estimates are affected by surface wave averaging, as well as inversion choices. We therefore also experimented with rescaling the geodynamic models to seismology first, before inverting for f . Resulting mixing patterns differ mostly in amplitude, but overall patterns are consistent.

We suggest that it is a useful exercise to use refined version of inversions for different LPO types to infer the melting and volatile content of the asthenosphere, e.g. as disturbed by plume activity (Karato, submitted for publication). The mixing patterns in Fig. 7 indicate, plausibly, that the regions underneath the ridges are relatively “dry”, while patches off to the west and east of the East Pacific Rise, where hotspots are found, appear to require modest ($f \sim 0.2$) amounts of LPO of the C-type fabric. Within North America, the western regions are inferred to have $f \sim 0.3$ compared to $f \sim 0$ toward the eastern margins where older lithosphere is found. To some extent, f anomalies will clearly trade off with wrong assumptions in the geodynamic starting model, such as poor choices for LVVs due to continental keels. The residual anisotropy appears, however, consistent with the presence of variable LPO fabrics. When interpreted in terms of volatile content in well constrained regions such as the Pacific basin, such analysis might provide new clues for our understanding of the nature of the asthenosphere (Karato, submitted for publication).

Residual radial anisotropy at larger depths, *i.e.* 250 km in the last row of Fig. 5, is dominated by an over-prediction of $\xi > 1$ structure in the western Pacific and underneath Australia. The mean $\langle \xi \rangle$ anisotropy signal is reduced to $\sim 25\%$ from the maximum at ~ 120 km depth (Fig. 4), which implies that $\delta\xi$ patterns at large depths might not be as well constrained seismologically as shallower regions. Residual anisotropy might arise due to

inadequate models of LVVs, in particular underneath continental regions. Another potential source of anisotropy mismatch, mainly underneath the Pacific plate, might be due to small-scale convection, which is not adequately incorporated in our large-scale flow computations. Horizontal shear-alignment is over-predicted (residual $\Delta\xi < 0$ regions in Fig. 5) roughly in regions where the seafloor is older than ~ 80 Ma. This number is consistent with the observed temporal onset of deviations from half-space cooling, as well as seismological evidence and geodynamic considerations on small-scale convection and reheating events (e.g. Zhong et al., 2007). A corresponding decrease of azimuthal anisotropy strength across the Pacific had been noted previously and associated with second-order convective features (Smith et al., 2004). However, the details of how asthenospheric, plate-shear patterns might be disrupted by lithospheric instabilities (Podolefsky et al., 2004; Smith et al., 2004) or plume-related (de-) hydration events (Karato, submitted for publication) remain to be determined.

5. Conclusions

Previously identified anomalous v_{SV} regions beneath the East Pacific Rise and relatively fast v_{SH} regions within the Pacific basin can be linked to mantle upwellings and shearing in the asthenosphere, respectively. Our results further validate the geodynamic reference model; major features in the Earth’s asthenosphere can be explained by applying laboratory-derived laws for olivine creep and LPO formation. Analysis of residual radial anisotropy yields evidence for shallow frozen-in structure in old continents that is consistent with a stochastic model of anisotropy. By inverting for different LPO types, maps of effective asthenospheric hydration-state can be created. Radial anisotropy can so help constrain mantle rheology, the degree of lateral viscosity variations, and possibly volatile content variations. Those are hard to infer from other geophysical data, but important for our understanding of tectonic processes including the nature of the asthenosphere, and the degree of plate-mantle coupling.

Acknowledgments

This manuscript benefited from the constructive criticism of three reviewers and our editor, Rob van der Hilst. We also thank

L. Moresi and S. Zhong for sharing CitcomS, which can be obtained from CIG (geodynamics.org), and E. Debayle, M. Panning, and M. Nettles for sharing their seismological models in electronic form. This work was supported by NSF grants EAR-0509722 and EAR-0643365, and computations were conducted at the University of Southern California Center for High Performance Computing and Communications (www.usc.edu/hpcc). Model *S362WMANI* is available online at <http://www.seismology.harvard.edu/~kustowski>, and anisotropy tools can be obtained from geodynamics.usc.edu. Most figures were produced with GMT (Wessel and Smith, 1991).

Appendix A

The patterns and amplitudes of seismic anisotropy in the upper mantle depend on two effects: First, the petrological composition of mantle rocks, and in particular the pressure, p , and temperature, T , dependence of the single crystal elastic constants. Second, the geographic orientation and nature of the LPO, in particular the degree of fabric saturation and the patterns of crystallographic axes ([100], [010], and [001]) resulting from dislocation creep depending on which slip systems are active (Karato et al., in press), see also Table 3. Petrological forward models were pioneered for single crystal estimates by Montagner and Anderson (1989), and explored in detail for LPO formation and azimuthal anisotropy by Becker et al. (2006a). Here, we briefly review these effects with focus on radial anisotropy and describe our petrological model.

We assume for simplicity that the entire upper mantle is made of olivine and enstatite (no crustal layer). Single crystal elasticity constants and their p , T derivatives are taken from the compilation by Estey and Douglas (1986), as newer measurements are only available for olivine. Background pressure is from PREM, and the background mantle temperature is an approximation to a half-space cooling profile from the surface down to 120 km where $T=1670$ °K, after which T increases along an adiabat to $T=2085$ °K at 420 km. The resulting depth-dependence of anisotropy symmetry-systems was pointed out by Browaeys and Chevrot (2004).

Fig. 8 shows radial anisotropy parameters for a single crystal with a 70/30% ol/en mix using Voigt averaging and horizontal alignment of the fast axis. Deviations from isotropy ($\xi=\phi=\eta=1$) are ~ 3 larger than what is mapped by seismology in terms of ξ (Fig. 4; corresponding velocity anomaly ratio ~ 1.7), as expected. The competing effects of temperature and pressure lead to a decrease of ξ from ~ 1.25 at 50 km to $\xi \sim 1.2$ at 400 km depth, a 20% variation (Fig. 8a). Fig. 8b shows the relative change in radially anisotropic wave speeds and anisotropy parameters with respect to temperature as a function of depth (obtained by finite differences). The strongest temperature dependence is displayed by $d \ln v_{SV}$, and $d \ln v_{PV}/d \ln v_{SV}$ decreases from ~ 0.75 at 50 km to ~ 0.7 at 400 km. For horizontally polarized waves, v_{PH} is predicted to be more temperature-sensitive than v_{SH} above ~ 250 km, and $d \ln v_{PH}/d \ln v_{SH}$ decreases from ~ 1.1 at 50 km to ~ 0.95 at 400 km. Based on our petrological model, scaling relationships for thermal effects of $d \ln v_{PV}/d \ln v_{SV} \sim 0.7$ and $d \ln v_{PH}/d \ln v_{SH} \sim 1$ are appropriate for the upper 400 km of the

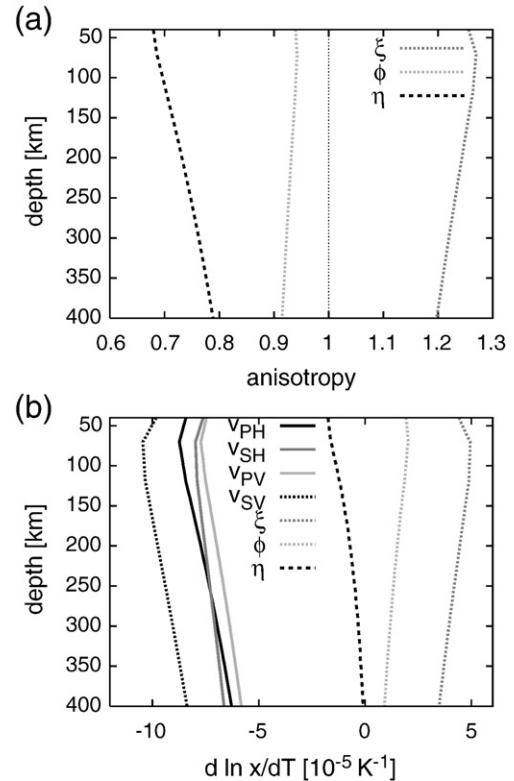


Fig. 8. Single crystal radial anisotropy (a, see Eq. (3)) and logarithmic temperature-derivatives (b, place holder “x” for velocities and anisotropy ratios) as a function of depth for a 70/30% mix of ol and en using a simplified background thermal structure as well as pressure increase from PREM. Elasticity constants are from Estey and Douglas (1986) and thermal expansivity $3 \cdot 10^{-5} \text{ K}^{-1}$. We show anisotropy for olivine fast axes aligned in the horizontal, [001] and [010] of enstatite aligned with [100] and [001] of olivine (cf. Montagner and Anderson, 1989; Becker et al., 2006a).

mantle. Given that the average Voigt v_S is twice as sensitive to SV than SH (Eq. (4)), the overall temperature dependence will, however, be such that $d \ln v_P/d \ln v_S < 1$, more in line with expectations from mineral physics. Given that $|d \ln v_{SV}/dT| \sim 1.3 |d \ln v_{SH}/dT|$, a temperature increase is expected to increase shear wave anisotropy ξ ; according to $d \ln \xi/dT \sim 5 \cdot 10^{-5} \text{ K}^{-1}$ temperature fluctuations of ± 200 °K correspond to ξ -variations of $\pm 1\%$.

If we were to include the effect of lateral temperature variations in our geodynamic anisotropy models as shown in Fig. 5, the main effect would be to increase ξ within oceanic regions by $\sim 0.5\%$ underneath the ridges compared to average regions (cf. Fig. 2). However, we neglect lateral $d \ln \xi/dT$ variations and only include the depth-dependence of elasticity parameters (Fig. 8a) because of mineral physics uncertainties and, more importantly, because the other sources of anisotropy variation, LPO orientation and saturation effects, are expected to dominate the signal by an order of magnitude (Montagner and Anderson, 1989). For example, if the dip of the single-crystal ol/en mix at 150 km depth varies by $\pm 45^\circ$ out of the horizontal, ξ and ϕ vary by $\pm 16\%$ and $\pm 12\%$, respectively. LPO saturation is expected to scale with the finite-strain accumulated during advective transport (Ribe, 1992; Kaminski and Ribe, 2001; Becker et al., 2006a), and one of the advantages of geodynamic flow models is that they can be used to predict typical

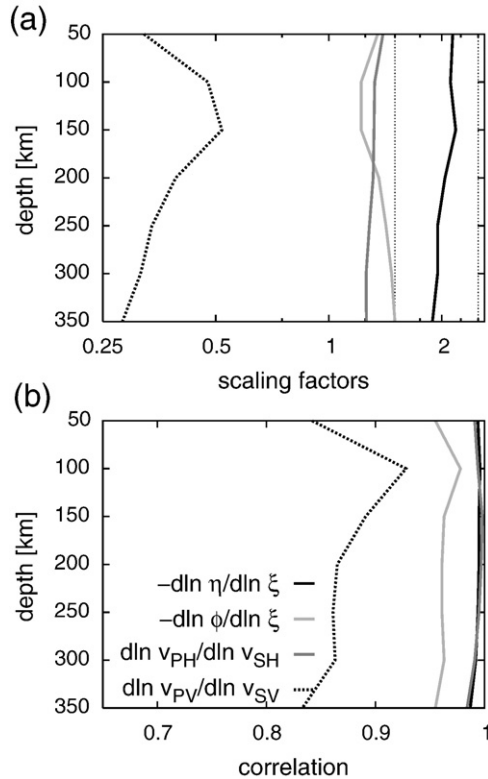


Fig. 9. LPO-based scaling relationships for radial anisotropy (a) and correlation between parameters (b) using the petrological model of Fig. 8 and our best-fit geodynamic model as shown in Fig. 5, without anisotropy variations due to temperature anomalies. Thin dashed lines in plot (a) mark the values of $d \ln \eta / d \ln \xi \sim -2.5$ and $d \ln \phi / d \ln \xi \sim -1.5$ as used by Panning and Romanowicz (2006) based on Montagner and Anderson (1989).

variations of both LPO orientations and saturation. From such models, one can derive LPO-based scaling relationships for anisotropic parameters. These can be employed for seismologic inversions once isotropic (*i.e.* temperature-dependent) variations of v_S and v_P are taken into account (Montagner and Anderson, 1989; Becker et al., 2006a).

Fig. 9 shows correlations and best-fit scaling relationships between radial anisotropy parameters computed from synthetic LPO samples at different layers of our preferred geodynamic model of Figs. 4a and 5, neglecting the effect of lateral temperature variations on anisotropy. Parameters η and ξ are highly correlated with correlation coefficients >0.95 , validating the idea that scaling relationships based on petrology may be of use for seismological inversions. The correlation is poorest between v_{PV} and v_{SV} , which corresponds to the reduction in $d \ln \phi / d \ln \xi$ correlation. The absolute values of the scaling relationships in Fig. 9a depend slightly on the viscosity structure used and the saturation strain, but variations in scaling factors are typically smaller than $\sim 10\%$. We find LPO-based scaling parameters of $d \ln \eta / d \ln \xi \sim -2$, and $d \ln \phi / d \ln \xi \sim -1.4$, $\sim 25\%$ lower than earlier estimates (Montagner and Anderson, 1989) as used for *SAW64AN* (Panning and Romanowicz, 2006). However, given the limited resolving power of seismology for ϕ and η , such differences are probably not large enough to warrant reanalysis. The *S* and *P* velocity scalings of Fig. 9 are $d \ln v_{PV} /$

$d \ln v_{SV} \sim 0.3$ and $d \ln v_{PH} / d \ln v_{SH} \sim 1.3$, $\sim 35\%$ lower and higher than the thermal derivatives, respectively. Therefore, $d \ln v_{PV} / d \ln v_{SV} = 0.55$ as used in *S362WMANI* is appropriate, while $d \ln v_{PH} / d \ln v_{SH} = 0.55$ is likely too low. As mentioned, we therefore performed additional inversions with $d \ln v_{PH} / d \ln v_{SH} = 1$, but found that the resulting ξ -anomalies are not significantly different from those used in the final *S362WMANI* as shown in Fig. 2. Moreover, the mean $\langle \eta \rangle$ structure we found for the new *S362WMANI* reference model, without constraining it to correlate with ξ *a priori*, is consistent with the amplitude co-variation as expected from the petrological model (cf. the match of $\langle \eta \rangle$ from geodynamics and seismology in Fig. 4).

We conclude that LPO orientation-derived scaling parameters such as in Fig. 9 appear to not be of crucial importance when used in global, surface wave dominated studies for present levels of data coverage. However, geodynamic estimates may still be useful for regional seismological inversions with different data sensitivities.

References

- Anderson, D.L., 1966. Recent evidence concerning the structure and composition of the Earth's mantle. *Physics and Chemistry of the Earth*, vol. 6. Pergamon Press, Oxford UK, pp. 1–131.
- Becker, T.W., O'Connell, R.J., 2001. Predicting plate velocities with geodynamic models. *Geochim. Geophys. Geosystems* 2 2001GC000171.
- Becker, T.W., Boschi, L., 2002. A comparison of tomographic and geodynamic mantle models. *Geochim. Geophys. Geosystems* 3 2001GC000168.
- Becker, T.W., 2006. On the effect of temperature and strain-rate dependent viscosity on global mantle flow, net rotation, and plate-driving forces. *Geophys. J. Int.* 167, 943–957.
- Becker, T.W., Kellogg, J.B., Ekström, G., O'Connell, R.J., 2003. Comparison of azimuthal seismic anisotropy from surface waves and finite-strain from global mantle-circulation models. *Geophys. J. Int.* 155, 696–714.
- Becker, T.W., Chevrot, S., Schulte-Pelkum, V., Blackman, D.K., 2006a. Statistical properties of seismic anisotropy predicted by upper mantle geodynamic models. *J. Geophys. Res.* 111. doi:10.1029/2005JB004095 B08309.
- Becker, T.W., Schulte-Pelkum, V., Blackman, D.K., Kellogg, J.B., O'Connell, R.J., 2006b. Mantle flow under the western United States from shear wave splitting. *Earth Planet. Sci. Lett.* 247, 235–251.
- Becker, T.W., Browaeys, J.T., Jordan, T.H., 2007a. Stochastic analysis of shear wave splitting length scales. *Earth Planet. Sci. Lett.* 259, 29–36.
- Becker, T.W., Ekström, G., Boschi, L., Woodhouse, J.W., 2007b. Length-scales, patterns, and origin of azimuthal seismic anisotropy in the upper mantle as mapped by Rayleigh waves. *Geophys. J. Int.* 171, 451–462.
- Beghein, C., Trampert, J., van Heijst, H.J., 2006. Radial anisotropy in seismic reference models of the mantle. *J. Geophys. Res.* 111. doi:10.1029/2005JB003772.
- Behn, M.D., Conrad, C.P., Silver, P.G., 2004. Detection of upper mantle flow associated with the African superplume. *Earth Planet. Sci. Lett.* 224, 259–274.
- Blackman, D.K., Kendall, J.-M., 2002. Seismic anisotropy of the upper mantle: 2. Predictions for current plate boundary flow models. *Geochim. Geophys. Geosystems* 3 2001GC000247.
- Boschi, L., Ekström, G., 2002. New images of the Earth's upper mantle from measurements of surface-wave phase velocity anomalies. *J. Geophys. Res.* 107.
- Boschi, L., Becker, T.W., Soldati, G., Dziewoński, A.M., 2006. On the relevance of born theory in global seismic tomography. *Geophys. Res. Lett.* 33. doi:10.1029/2005GL025063 L06302.
- Browaeys, J., Chevrot, S., 2004. Decomposition of the elastic tensor and geophysical applications. *Geophys. J. Int.* 159, 667–678.
- Čadež, O., Fleitout, L., 2003. Effect of lateral viscosity variations in the top 300 km of the mantle on the geoid and dynamic topography. *Geophys. J. Int.* 152, 566–580.

- Chastel, Y.B., Dawson, P.R., Wenk, H.-R., Bennett, K., 1993. Anisotropic convection with implications for the upper mantle. *J. Geophys. Res.* 98, 17757–17771.
- Christensen, U.R., 1987. Some geodynamical effects of anisotropic viscosity. *Geophys. J. R. Astr. Soc.* 91, 711–736.
- Conrad, C.P., Lithgow-Bertelloni, C., 2006. Influence of continental roots and asthenosphere on plate-mantle coupling. *Geophys. Res. Lett.* 33. doi:10.1029/2005GL02562.
- Conrad, C.P., Behn, M.D., Silver, P.G., 2007. Global mantle flow and the development of seismic anisotropy: differences between the oceanic and continental upper mantle. *J. Geophys. Res.* 112. doi:10.1029/2006JB004608.
- Debayle, E., Kennett, B.L.N., Priestley, K., 2005. Global azimuthal seismic anisotropy and the unique plate-motion deformation of Australia. *Nature* 433, 509–512.
- de Bresser, J.H.P., ter Heege, J.H., Spiers, C.H., 2001. Grain size reduction by dynamic recrystallization: can it result in major rheological weakening? *Int. J. Earth Sci.* 90, 28–45.
- Dziewoński, A.M., Anderson, D.L., 1981. Preliminary reference Earth model. *Phys. Earth Planet. Inter.* 25, 297–356.
- Ekström, G., Dziewoński, A.M., 1998. The unique anisotropy of the Pacific upper mantle. *Nature* 394, 168–172.
- Estey, L.H., Douglas, B.J., 1986. Upper mantle anisotropy: a preliminary model. *J. Geophys. Res.* 91, 11393–11406.
- Fouch, M.J., Rondenay, S., 2006. Seismic anisotropy beneath stable continental interiors. *Phys. Earth Planet. Inter.* 158, 292–320.
- Gaboret, C., Forte, A.M., Montagner, J.-P., 2003. The unique dynamics of the Pacific Hemisphere mantle and its signature on seismic anisotropy. *Earth Planet. Sci. Lett.* 208, 219–233.
- Gaherty, J.B., Jordan, T.H., 1995. Lehmann discontinuity as the base of an anisotropic layer beneath continents. *Science* 268, 1468–1471.
- Gung, Y., Panning, M., Romanowicz, B., 2003. Global anisotropy and the thickness of continents. *Nature* 422, 707–711.
- Gu, Y.H., Lerner-Lam, A.L., Dziewoński, A.M., Ekström, G., 2005. Deep structure and seismic anisotropy beneath the East Pacific Rise. *Earth Planet. Sci. Lett.* 232, 259–272.
- Hager, B.H., O'Connell, R.J., 1981. A simple global model of plate dynamics and mantle convection. *J. Geophys. Res.* 86, 4843–4867.
- Hirth, G., Kohlstedt, D.L., 2004. Rheology of the upper mantle and the mantle wedge: a view from the experimentalists. In: Eiler, J. (Ed.), *Inside the Subduction Factory*. Geophysical Monograph, vol. 138. American Geophysical Union, Washington DC, pp. 83–105.
- Ito, G., Shen, Y., Hirth, G., Wolfe, C.J., 1999. Mantle flow, melting, and dehydration of the Iceland mantle plume. *Earth Planet. Sci. Lett.* 165, 81–96.
- Jordan, T.H., 1981. Global tectonic regionalization for seismological data analysis. *Bull. Seismol. Soc. Am.* 71, 1131–1141.
- Kaminski, É., 2002. The influence of water on the development of lattice preferred orientation in olivine aggregates. *Geophys. Res. Lett.* 29. doi:10.1029/2002GL014710.
- Kaminski, É., Ribe, N.M., 2001. A kinematic model for recrystallization and texture development in olivine polycrystals. *Earth Planet. Sci. Lett.* 189, 253–267.
- Kaminski, É., Ribe, N.M., Browaeys, J.T., 2004. D-Rex, a program for calculation of seismic anisotropy due to crystal lattice preferred orientation in the convective upper mantle. *Geophys. J. Int.* 157, 1–9.
- Karato, S.-I., 1992. On the Lehmann discontinuity. *Geophys. Res. Lett.* 51, 2255–2258.
- Karato, S.-I., 1998. Seismic anisotropy in the deep mantle, boundary layers and the geometry of convection. *Pure Appl. Geophys.* 151, 565–587.
- Karato, S.-I., submitted for publication. The nature of plume–upper mantle interaction inferred from geophysical anomalies in the Pacific. *Nature Geosciences*.
- Karato, S.-I., Jung, H., Katayama, I., Skemer, P., in press. Geodynamic significance of seismic anisotropy of the upper mantle: new insights from laboratory studies. *Ann. Rev. Earth Planet. Sci.* doi:10.1146/annurev.earth.36.031207.124120.
- Kustowski, B., Ekström, G., Dziewoński, A.M., submitted for publication. The anisotropic shear-wave velocity structure of the Earth's mantle: a global model. *J. Geophys. Res.*
- Laske, G., Masters, G., 1998. Surface-wave polarization data and global anisotropic structure. *Geophys. J. Int.* 132, 508–520.
- Lassak, T.M., Fouch, M.J., Hall, C.E., Kaminski, E., 2006. Seismic characterization of mantle flow in subduction systems: can we resolve a hydrated mantle wedge? *Earth Planet. Sci. Lett.* 243, 632–649.
- Lee, C.-T.A., Lenardic, A., Cooper, C.M., Niu, F., Levander, A., 2005. The role of chemical boundary layers in regulating the thickness of continental and oceanic thermal boundary layers. *Earth Planet. Sci. Lett.* 230, 379–395.
- Mainprice, D., Tommasi, A., Couvy, H., Cordier, P., Frost, N.J.J., 2005. Pressure sensitivity of olivine slip systems and seismic anisotropy of Earth's upper mantle. *Nature* 433, 731–733.
- McKenzie, D.P., 1979. Finite deformation during fluid flow. *Geophys. J. R. Astr. Soc.* 58, 689–715.
- McNamara, A.K., van Keken, P.E., Karato, S.I., 2002. Development of anisotropic structure in the Earth's lower mantle by solid-state convection. *Nature* 416, 310–314.
- Montagner, J.-P., Nataf, H.-C., 1986. A simple method for inverting the azimuthal anisotropy of surface waves. *J. Geophys. Res.* 91, 511–520.
- Montagner, J.-P., Anderson, D.L., 1989. Petrological constraints on seismic anisotropy. *Phys. Earth Planet. Inter.* 54, 82–105.
- Montagner, J.-P., Tanimoto, T., 1991. Global upper mantle tomography of seismic velocities and anisotropies. *J. Geophys. Res.* 96, 20337–20351.
- Montagner, J.-P., 1998. Where can seismic anisotropy be detected in the Earth's mantle? In: *boundary layers*. *Pure Appl. Geophys.* 151, 223–256.
- Montagner, J.-P., 2002. Upper mantle low anisotropy channels below the Pacific plate. *Earth Planet. Sci. Lett.* 202, 263–274.
- Moresi, L., Solomatov, V.S., 1995. Numerical investigations of 2D convection with extremely large viscosity variations. *Phys. Fluids* 7, 2154–2162.
- Nataf, H.-C., Nakanishi, I., Anderson, D.L., 1986. Measurements of mantle wave velocities and inversion for lateral heterogeneities and anisotropy. Part III. Inversion. *J. Geophys. Res.* 91, 7261–7307.
- Nettles, M., Dziewoński, A.M., 2008. Radially anisotropic shear velocity structure of the upper mantle globally and beneath North America. *J. Geophys. Res.* 113, B02303. doi:10.1029/2006JB004819.
- Nicolas, A., Christensen, N.I., 1987. Formation of anisotropy in upper mantle peridotites; a review. In: Fuchs, K., Froidevaux, C. (Eds.), *Composition, Structure and Dynamics of the Lithosphere–Asthenosphere System*, vol. 16 of *Geodynamics*. American Geophysical Union, Washington DC, pp. 111–123.
- Panning, M., Romanowicz, B., 2006. A three-dimensional radially anisotropic model of shear velocity in the whole mantle. *Geophys. J. Int.* 167, 361–379.
- Podolefsky, N.S., Zhong, S., McNamara, A.K., 2004. The anisotropic and rheological structure of the oceanic upper mantle from a simple model of plate shear. *Geophys. J. Int.* 158, 287–296.
- Regan, J., Anderson, D.L., 1984. Anisotropic models of the upper mantle. *Phys. Earth Planet. Inter.* 35, 227–263.
- Ribe, N.M., 1992. On the relation between seismic anisotropy and finite strain. *J. Geophys. Res.* 97, 8737–8747.
- Shapiro, N.M., Ritzwoller, M.H., 2002. Monte-Carlo inversion for a global shear velocity model of the crust and upper mantle. *Geophys. J. Int.* 151, 88–105.
- Silver, P.G., 1996. Seismic anisotropy beneath the continents: probing the depths of geology. *Ann. Rev. Earth Planet. Sci.* 24, 385–432.
- Smith, D.B., Ritzwoller, M.H., Shapiro, N.M., 2004. Stratification of anisotropy in the Pacific upper mantle. *J. Geophys. Res.* 109. doi:10.1029/2004JB003200.
- Steinberger, B., 2000. Plumes in a convecting mantle: models and observations for individual hotspots. *J. Geophys. Res.* 105, 11127–11152.
- Tanimoto, T., Anderson, D.L., 1984. Mapping convection in the mantle. *Geophys. Res. Lett.* 11, 287–290.
- Tommasi, A., Mainprice, D., Canova, G., Chastel, Y., 2000. Viscoplastic self-consistent and equilibrium-based modelling of olivine lattice preferred orientation. I. Implications for the upper mantle seismic anisotropy. *J. Geophys. Res.* 105, 7893–7908.
- Trampert, J., van Heijst, H.J., 2002. Global azimuthal anisotropy in the transition zone. *Science* 296, 1297–1299.
- Trampert, J., Spetzler, J., 2006. Surface wave tomography: finite frequency effects lost in the null space. *Geophys. J. Int.* 164, 394–400.
- Wenk, H.-R., Tomé, C.N., 1999. Modeling dynamic recrystallization of olivine aggregates deformed in simple shear. *J. Geophys. Res.* 104, 25513–25527.

- Wenk, H.-R., Speziale, S., McNamara, A.K., Garnero, E.J., 2006. Modeling lower mantle anisotropy development in a subducting slab. *Earth Planet. Sci. Lett.* 245, 302–314.
- Wessel, P., Smith, W.H.F., 1991. Free software helps map and display data. *EOS Trans. AGU* 72, 445–446.
- Wookey, J., Kendall, J.-M., Barruol, G., 2002. Mid-mantle deformation inferred from seismic anisotropy. *Nature* 415, 777–780.
- Zhong, S., Zuber, M.T., Moresi, L., Gurnis, M., 2000. Role of temperature-dependent viscosity and surface plates in spherical shell models of mantle convection. *J. Geophys. Res.* 105, 11063–11082.
- Zhou, Y., Ritzwoller, M., Shapiro, N., Landuyt, W., Huang, J., Wessel, P., 2007. Bathymetry of the Pacific plate and its implications for thermal evolution of lithosphere and mantle dynamics. *J. Geophys. Res.* 112, B06412. doi:10.1029/2006JB004628.
- Zhou, Y., Nolet, G., Dahlen, F.A., Laske, G., 2006. Global upper-mantle structure from finite-frequency surface-wave tomography. *J. Geophys. Res.* 111. doi:10.1029/2005JB003677.